

SPARSE ARRAY MICROWAVE 3-D IMAGING: COMPRESSED SENSING RECOVERY AND EXPERIMENTAL STUDY

S.-J. Wei*, X.-L. Zhang, J. Shi, and K.-F. Liao

School of Electronic Engineering, University of Electronic Science and Technology of China, Chengdu 611731, China

Abstract—Microwave array 3-D imaging is an emerging technique capable of producing a 3-D map of scattered electric fields. Its all-weather and large scene imaging features make it an attractive powerful tool for target detection and feature extraction. Typically, a microwave array 3-D imaging system based on the classical sampling theory requires a large dense 2-D antenna array, which may suffer from a very high cost. To reduce the number of the antenna array elements, this paper surveys the use of compressed sensing recovery and sparse measurement strategies for microwave array 3-D imaging. Combining with the typical spatial sparsity of the underlying scene, we pose the sparse array microwave 3-D imaging as finding sparse solutions to under-determined linear equations. Further, to reduce the computational of the compressed sensing recovery with the large-scale echoes data, we divide the underlying 3-D scene into a series of equal-range 2-D slices, and deal with these slices separately using the orthogonal matching pursuit (OMP) algorithm. Lastly, the performance of the presented compressed sensing approach is verified by an X-band microwave array 3-D imaging system. The experimental results demonstrate that the compressed sensing approach can produce a better resolution 3-D image of the observed scatterers compared with the conventional method, especially in the case of very sparse activate antenna array.

Received 23 August 2012, Accepted 15 October 2012, Scheduled 18 December 2012

* Corresponding author: Shun-Jun Wei (grinwshj@163.com).

1. INTRODUCTION

Microwave 3-D imaging is an emerging active-imaging technology that is able to produce high-resolution 3-D images of the electromagnetic scattering coefficients of the underlying targets. With all-time, large scene and contactless observing capability and operation under all-weather, microwave 3-D imaging has become an attractive and powerful tool in many civilian military and biomedical applications, such as remote sensing [1], object detection and tracking [2], concealed weapon detection [3], through-barrier imaging [4], non-destructive pipeline imaging [5], breast cancer imaging [6] and magnetic induction tomography [7, 8], etc.. Moreover, how to obtain high resolution microwave 3-D images of the scatterers is also a hot topic in the radar community recently [9–11]. Generally, a microwave 3-D imaging system uses a 2-D antenna array to produce the 2-D resolution in the antenna array plane, utilizes the pulse compression technique to obtain the range resolution. To obtain a high-quality 3-D image, a large dense 2-D real or virtual array antenna is usually required. However, such a large dense 2-D array cannot be easily applied or synthesized due to the limited system size and the limited observing time in practice. Furthermore, the use of such a dense array may result in both high cost and large storage problems for the imaging system. These motivate development of an effective microwave 3-D imaging system that requires only a sparse antenna array. In [12], we presented a “one-active” linear array antenna microwave 3-D imaging technique, and successfully developed a sparse array microwave 3-D imaging system. The system controls the motions of the only two antennas, one transmitter and one receiver, to synthesize the desired virtual 2-D array antenna. After a series of experiments, the first field experimental results of this “one-active” microwave array 3-D imaging system, obtained by the 3-D back-projection method, were presented in [13]. The experiments demonstrated that the produced images can well capture the domain 3-D scattering features of the observed targets. However, we also found that when the synthetic 2-D antenna array was very sparse, the performance of the back-projection method would be serious degradation, which was interfered by very high side-lobes.

Unlike 1-D and 2-D microwave image, 3-D microwave image usually exhibits spatial sparsity. Hence, microwave 3-D imaging is typically an inverse scattering problem whereby a map of the reflectivity is reconstructed from the echo measurements of scattering field, this task can be posed as finding sparse solutions to the linear equations. However, the classical methods for 3-D microwave imaging, such as the 3-D back-projection algorithm [1, 10], the 3-D range

migration algorithm [14], the chirp scaling algorithm [15], the 3-D omega-k algorithm [16] and the wave-number domain algorithm [17], etc., never exploit such prior sparsity knowledge. In addition, the resolutions of these conventional algorithms are limited by classical radar uncertainty principle. If the echo signal sampling rate doesn't satisfy the Nyquist rate, these conventional methods will suffer from image degradation and artifacts. These limitations make it difficult to use conventionally reconstructed images for robust target detection and recognition.

Compressed sensing (CS), an emerging theory of signal processing, indicates that the sparse signal can be exactly recovered by incoherent linear projection using just a small number of random measurements. Recently, CS has been widely discussed and studied in different fields, such as medical imaging [18], communications [19] and image reconstruction [20], etc.. Some CS sparse recovery algorithms have also been successfully developed for microwave imaging [21–27]. E.g., in [28], a new approach based the contrast field formulation of the microwave imaging problem that exploits the Bayesian compressive sampling paradigm is proposed for the reconstruction of sparse distributions of weak scatterers. In [29], we proposed a sparse recovery approach based on CS for linear array synthetic aperture radar imaging, and the numerical simulation results indicated that CS approach offered many advantages such as super-resolution and feature enhancement compared with the conventional methods.

In this paper, we survey the use of CS recovery and sparse measurement strategies in microwave array 3-D imaging. Exploiting the spatial sparsity of the observed scene, we convert the sparse array microwave 3-D imaging into an ill-posed linear inverse problem with a small number of measurements. Furthermore, a modified OMP algorithm, without requiring the signal sparsity as the prior knowledge, is presented to recover the sparse reflectivity of the observed scatterers. In order to reduce the computational of the large-scale echo processing, we divide the 3-D scene into a series of equal-range 2-D slices, and deal with each slice separately. In addition, with the point spread function of echo signal, we investigate the relationship between the interval of adjacent scene cells and the mutual coherence of the measured matrix. Finally, some different types of targets are test by the developed microwave array imaging system to demonstrate the advantages of the presented CS algorithm. The results show that high resolution 3-D images can be obtained by a very sparse array antenna with CS method, which may pave the way for microwave 3-D imaging in many new applications that require a small sparse array antenna and high-resolution image, such as radar cross section (RCS) measurement and

electromagnetic feature extraction, etc..

The rest of this paper is constructed as follows. In Section 2, we introduce the sparse array microwave 3-D imaging model and sketch its image formation as a linear inverse problem. In Section 3, the basic theory of CS is described and the OMP algorithm is proposed for the sparse array microwave 3-D imaging. Experimental results are presented in Section 4 along with the performance analysis. Finally, we summarize the results of the paper in Section 5.

2. SIGNAL MODEL AND PROBLEM FORMULATION

2.1. System Geometric Model

The simple geometric model of the sparse array microwave 3-D imaging is illustrated in Figure 1(a). The sparse 2-D antenna array can be a real array or a virtual array synthesized by the synthetic techniques, e.g., single input multiple output (SIMO) technique and multiple input multiple output (MIMO) technique [26]. The positions of the total array elements are described by a transducer set \mathbf{P}_{tr} .

$$\mathbf{P}_{tr} = \{\mathbf{P}_n | \mathbf{P}_n = \langle x_n, y_n, z_n \rangle; n \in \Upsilon\} \quad (1)$$

where, $\Upsilon = \{1, 2, \dots, N\}$ denotes the index set, N denotes the total number of the array elements.

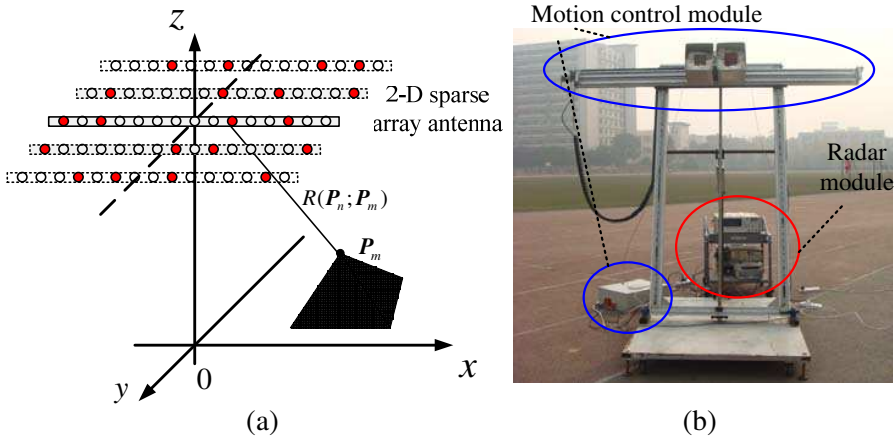


Figure 1. The geometric model and the experimental system of the sparse array microwave 3-D imaging. (a) The geometric model. (b) The experimental system.

In order to reduce the number of transmit/receive devices and on-board storage equipments in the system, we control the motions of the transmitter and the receiver antennas to synthesize a virtual 2-D antenna array in this paper. In particular, we have successfully developed an X-band microwave 3-D imaging system, as shown in Figure 1(b). The imaging system consists of two parts: the radar module and the motion-control module. The radar module mainly transmits a linear frequency modulated (LFM) signal toward an area of interest, and receives the echoes from the observed targets. The motion-control module mainly controls the motions of the transmitter and the receiver antennas on a 2-D rail to synthesize the desired virtual 2-D antenna array. In addition, the motion control module consists of a set of high-precision transfer devices, position measured devices and high-precision motors, which can record the positions of the transmitter and the receiver antennas during the motions [12, 13].

2.2. Signal Model

We assume that a point target is located at position $\mathbf{P}_m = \langle x_m, y_m, z_m \rangle$ with scattering coefficient σ_m . Then the slant range from this scatterer \mathbf{P}_m to the n th antenna array element at position \mathbf{P}_n can be written as

$$R(\mathbf{P}_n, \mathbf{P}_m) = \|\mathbf{P}_n - \mathbf{P}_m\|_2, \quad n = 1, 2, \dots, N \quad (2)$$

where, $\|\cdot\|_p$ denotes the p -norm of vector.

Suppose that the radar system transmits a LFM signal, the received echo of the n th element for the point scatterer \mathbf{P}_m can be expressed as follows

$$S(t; \mathbf{P}_n, \mathbf{P}_m) = \sigma_m \exp(-j2\pi f_c \tau(\mathbf{P}_n, \mathbf{P}_m)) \exp[j\pi f_{dr}(t - \tau(\mathbf{P}_n, \mathbf{P}_m))^2], \quad |t| \in T/2 \quad (3)$$

where t denotes the fast-time, f_c denotes the carrier frequency, f_{dr} is the LFM chirp rate and T denotes the pulse repetition period, $\tau(\mathbf{P}_n, \mathbf{P}_m) = 2R(\mathbf{P}_n, \mathbf{P}_m)/C$ denotes the echo delay of the scatterer \mathbf{P}_m , C is the speed of light in air. After range focusing by the pulse compression technique, the focused echo signal can be written as

$$S_c(r; \mathbf{P}_n, \mathbf{P}_m) = \sigma_m \chi_R(r - R(\mathbf{P}_n, \mathbf{P}_m)) \exp(-j2kR(\mathbf{P}_n, \mathbf{P}_m)), \quad n = 1, 2, \dots, N \quad (4)$$

where r denotes the range domain, $k = 2\pi f_c/C$ denotes the wave number, $\chi_R(r - R(\mathbf{P}_n, \mathbf{P}_m))$ denotes the range ambiguity function at range cell r . For a multiple-scatterers scene, the echoes signal is the

sum of all scatterers, i.e.,

$$\begin{aligned} S_c(r, \mathbf{P}_n) &= \sum_{m \in \mathbf{\Pi}} S_c(r; \mathbf{P}_n, \mathbf{P}_m) \\ &= \sum_{m \in \mathbf{\Pi}} f(r; \mathbf{P}_n, \mathbf{P}_m) \exp(-j2kR(\mathbf{P}_n, \mathbf{P}_m)) \end{aligned} \quad (5)$$

where, $f(r; \mathbf{P}_n, \mathbf{P}_m) = \sigma_m \chi_R(r - R(\mathbf{P}_n, \mathbf{P}_m))$ denotes the range compression reflectivity at range cell r , $\mathbf{\Pi} = \{1, 2, \dots, M\}$ denotes the scatterers index set in each equiv-range slice. We can parameterize (5) in terms of the reflectivity vector $\mathbf{f}(r)$ and the delay-phase function $\boldsymbol{\psi}(r, \mathbf{P}_n)$ as follows.

$$S_c(r, \mathbf{P}_n) = \boldsymbol{\psi}(r, \mathbf{P}_n)^T \mathbf{f}(r) \quad (6)$$

where, $\boldsymbol{\psi}(r, \mathbf{P}_n) = \{\psi_j | \psi_j = \exp(-j2kR(\mathbf{P}_n, \mathbf{P}_j)), j \in \mathbf{\Pi}\}$ is interpreted as an M -elements measurement vector, $\mathbf{f}(r) = \{f_j | f_j = f(r; \mathbf{P}_n, \mathbf{P}_j), j \in \mathbf{\Pi}\}$ denotes an M -elements reflectivity coefficient vector at range cell r . Further, we rearrange the range focusing signal $S_c(r, \mathbf{P}_n)$ into an N -element vector, i.e.,

$$\mathbf{S}_c(r) = [S_c(r, 1), S_c(r, 2), \dots, S_c(r, N)]^T \quad (7)$$

When we take an additive noise $\boldsymbol{\nu}$ (e.g., assuming a white Gaussian noise with zero-mean and variance $\boldsymbol{\Sigma}$) into account, the relationship between the scattering coefficient vector $\mathbf{f}(r)$ and the observed signal vector $\mathbf{S}_c(r)$ can be compactly written as a linear representation model

$$\mathbf{S}_c(r) = \mathbf{A}(r) \mathbf{f}(r) + \boldsymbol{\nu} \quad (8)$$

where $\mathbf{A}(r) \in \mathbb{C}^{N \times M}$ denotes the measurement matrix of the range-compression signal at range cell r , which can be expressed as a form of partial Fourier basis matrix as follows.

$$\begin{aligned} \mathbf{A}(r) &= \left[\boldsymbol{\psi}(r, \mathbf{P}_1)^T, \boldsymbol{\psi}(r, \mathbf{P}_2)^T, \dots, \boldsymbol{\psi}(r, \mathbf{P}_N)^T \right]^T \\ &= \begin{bmatrix} \exp(-j2kR(\mathbf{P}_1, \mathbf{P}_1)) & \exp(-j2kR(\mathbf{P}_1, \mathbf{P}_2)) \\ \exp(-j2kR(\mathbf{P}_2, \mathbf{P}_1)) & \exp(-j2kR(\mathbf{P}_2, \mathbf{P}_2)) \\ \vdots & \vdots \\ \exp(-j2kR(\mathbf{P}_N, \mathbf{P}_1)) & \exp(-j2kR(\mathbf{P}_N, \mathbf{P}_2)) \\ \dots & \exp(-j2kR(\mathbf{P}_1, \mathbf{P}_M)) \\ \dots & \exp(-j2kR(\mathbf{P}_2, \mathbf{P}_M)) \\ \vdots & \vdots \\ \dots & \exp(-j2kR(\mathbf{P}_N, \mathbf{P}_M)) \end{bmatrix} \end{aligned} \quad (9)$$

From (8), we can see that the objective of microwave array 3-D imaging is to estimate the reflectivity vector $\mathbf{f}(r)$ from a linear

equation with the given measurement matrix $\mathbf{A}(r)$ and the measured signal $\mathbf{S}_c(r)$. Since the 2-D antenna array is sparse activate, the row number N of the measurement matrix $\mathbf{A}(r)$ will be much smaller than the column number M . Therefore, the sparse array microwave 3-D imaging is typically an ill-posed linear inverse problem. Conventional match-filter-based methods mainly resolve such an ill-posed linear equation through the adjoint matrix of the Fourier transformation $\hat{\mathbf{f}}(r) = \mathbf{A}(r)^H \mathbf{S}_c(r)$. However, the estimated signal $\hat{\mathbf{f}}(r)$ is definitely not equal to the original signal $\mathbf{f}(r)$ because $\mathbf{A}(r)^H \mathbf{A}(r) \neq \mathbf{I}$, and an error $(\mathbf{A}(r)^H \mathbf{A}(r) - \mathbf{I})\mathbf{S}_c(r)$ is unavoidable. So the conventional match-filter-based methods always suffer from important shortcomings, such as resolution limitation to the array length and sidelobe artifacts.

3. COMPRESSED SENSING IMAGING

3.1. Basic Theory of Compressed Sensing

Compressed sensing (CS) enables the reconstruction of sparse signal using a much smaller number of measurements than that under Nyquist rate [30]. Assume that a vector $\mathbf{x} \in \mathbb{C}^M$ has a sparse representation $\mathbf{x} = \mathbf{\Psi}\boldsymbol{\alpha}$ in terms of basis matrix $\mathbf{\Psi} \in \mathbb{C}^{M \times M}$, and only $K \ll M$ out of M coefficients $\boldsymbol{\alpha}$ are nonzero. A signal \mathbf{y} is obtained from a noisy linear measurement $\mathbf{y} = \mathbf{\Phi}\mathbf{x} + \mathbf{n} \in \mathbb{C}^N$, where $\mathbf{\Phi} \in \mathbb{C}^{N \times M}$ donates the sensing matrix and $N \ll M$. Obviously, this equation is an ill-posed inverse problem and has infinitely many solutions. To find the sparse unique resolution of the ill-posed linear equation, the approaches from CS theory mainly recover the sparse signal $\boldsymbol{\alpha}$ via a convex optimization based on l_1 norm.

$$\hat{\boldsymbol{\alpha}} = \arg \min_{\boldsymbol{\alpha}} \|\boldsymbol{\alpha}\|_1 \text{ s.t. } \|\mathbf{y} - \mathbf{\Phi}\mathbf{\Psi}\boldsymbol{\alpha}\|_2 < \varepsilon \tag{10}$$

where ε bounds the amount of noise in the measured data \mathbf{y} . In [31], E. J. Candes indicated that CS can reconstruct the sparse signal exactly if the measurement matrix $\mathbf{\Phi}\mathbf{\Psi}$ satisfies some certain properties. One of such properties is the Restricted Isometry Property (RIP), which requires that

$$(1 - \delta_K) \|\boldsymbol{\chi}\|_2^2 \leq \|\mathbf{\Phi}\mathbf{\Psi}\boldsymbol{\chi}\|_2^2 \leq (1 + \delta_K) \|\boldsymbol{\chi}\|_2^2 \tag{11}$$

for all vector $\boldsymbol{\chi}$ such that $\|\boldsymbol{\chi}\|_0 \leq K$, the restricted isometry constants $\delta_K \in (0, 1)$. The smaller δ_K value means that the sparse signal can be better reconstructed. The RIP is closely related to an incoherency property. When the number of samples N is large, estimating and testing the RIP is impractical. A tractable bound on the RIP can be

obtained through the mutual coherence, which is defined as

$$\mu(\Phi\Psi) = \max_{i,j,i \neq j} |\langle \varphi_i, \varphi_j \rangle| / (\|\varphi_i\|_2 \|\varphi_j\|_2) \quad (12)$$

where φ_i denotes the i th column from the measurement matrix $\Phi\Psi$. It has been shown in [31] that the restricted isometry constants satisfy the bound $\delta_k \leq (k-1)\mu$ well with the mutual coherence μ .

In microwave imaging, if the underlying scene exhibits spatial sparsity, the basis matrix in (10) can be selected as the identity matrix $\Psi = \mathbf{I}$. In this case, the mutual coherence $\mu(\Phi\Psi)$ for microwave array imaging only depends on the sensing matrix Φ , which is expressed as the partial Fourier matrix $\Phi = \mathbf{A}(r)$ as mentioned in Section 2. Hence, we have $\mu(\Phi\Psi) = \mu(\mathbf{A}(r))$. From (6) and (9), we can clearly see that the i th column of the matrix $\mathbf{A}(r)$ is corresponding to the phase-delay function for the i th scene cell, which can be expressed as

$$\varphi_i = [\exp(-j2kR(\mathbf{P}_1, \mathbf{P}_i)), \exp(-j2kR(\mathbf{P}_2, \mathbf{P}_i)), \dots, \exp(-j2kR(\mathbf{P}_N, \mathbf{P}_i))] \quad (13)$$

Submitting (13) into (12), the mutual coherence of the measurement matrix $\mathbf{A}(r)$ in microwave array imaging can be written as

$$\mu(\mathbf{A}(r)) = \max_{i,j,i \neq j} \left| \sum_{n=1}^N \exp[-j2k(R(\mathbf{P}_n, \mathbf{P}_i) - R(\mathbf{P}_n, \mathbf{P}_j))] \right| / N \quad (14)$$

Obviously, if the system parameters are fixed, the mutual $\mu(\mathbf{A}(r))$ only depends on the interval of the underlying scene grids $\Delta R_{ij} = R(\mathbf{P}_n, \mathbf{P}_i) - R(\mathbf{P}_n, \mathbf{P}_j)$ and the position distribution \mathbf{P}_n of the 2-D array antenna elements. To reconstruct successfully by CS theory, we need to select a proper interval of the scene grids and design a suitable sparse 2-D antenna array so that the measurement matrix $\mathbf{A}(r)$ is sufficient incoherent. E. J. Candes showed that the low coherence of a partial Fourier matrix can be achieved by randomly select N rows of the $M \times M$ Fourier matrix [32]. According to this idea, a sparse array antenna with its elements obeyed by random distribution is employed to achieve low coherence in our experiments. The relationship between the mutual coherence and the interval of the scene grids will be discussed in Section 4.

3.2. Orthogonal Matching Pursuit Reconstruction

According to (10), given the measured echo signal $\mathbf{S}_c(r)$ and the measurement matrix $\mathbf{A}(r)$, the sparse reflectivity of the 3-D underlying scene $\mathbf{f}(r)$ can be recovered by CS as follows.

$$\mathbf{f}(r) = \arg \min_{\mathbf{f}(r)} \|\mathbf{f}(r)\|_1 \quad \text{s.t.} \quad \|\mathbf{S}_c(r) - \mathbf{A}(r)\mathbf{f}(r)\|_2 < \varepsilon \quad (15)$$

Recently, there are at least three classes of CS reconstruction approaches [33], including l_p norm regularization algorithms, greedy algorithms and iteratively least squares algorithms, have been developed to solving the ill-posed linear inverse problem. In this paper, a well known greedy algorithm, named as orthogonal matching pursuit (OMP) [34], is used to recover the sparse 3-D images of the illuminated targets. The OMP algorithm is an iterative procedure, an atom is selected and a residual is updated in each iteration. The next selected atom is the one which maximizes the correlation with the current residual. The pseudo-code for the OMP algorithm is summarized in Algorithm 1. In this paper, the basis matrix Ψ in Algorithm 1 is selected as the identity matrix, and the measurement matrix Φ is expressed as the partial Fourier basis matrix $\mathbf{A}(r)$.

Algorithm 1: Orthogonal matching pursuit (OMP).

Inputs: measurement matrix Φ , basis matrix Ψ , measurements \mathbf{y} .

Outputs: K -sparse approximation α , reflectivity vector \mathbf{x} .

Initialize: $\alpha^{(0)} = 0$, $\mathbf{r}^{(0)} = \mathbf{y}$, $n = 0$, $\Omega^{(0)} = \phi$

while halting criterion false **do**

$$k^{(n)} = \arg \max_k \|\phi_k^T \mathbf{r}^{(n-1)}\|_2 \quad \{\text{atom selection}\}$$

$$\Omega^{(n)} = \Omega^{(n-1)} \cup k^{(n)}$$

$$\alpha^{(n)} = (\Phi \Psi)_{\Omega^{(n)}}^H \mathbf{y} \quad \{\text{signal estimation}\}$$

$$\mathbf{r}^{(n)} = \mathbf{y} - \Phi \Psi \alpha^{(n)} \quad \{\text{measurement residual updated}\}$$

$$n \leftarrow n + 1$$

end while

return $\alpha \leftarrow \alpha^{(n)}$, $\mathbf{x} = \Psi \alpha$

To recover exactly by the OMP algorithm, the sparsity K of the original signal is usually selected as the iteration number. However, the sparsity K of the observed scene is impossible to be exactly known in microwaving imaging. To stop the OMP iteration procedure and guarantee the performance, an iteration condition based on the reconstruction error $E = \|\alpha^{(n)} - \alpha^{(n-1)}\| / \|\alpha^{(n)}\|$ is used in this paper, where $\alpha^{(n)}$ denotes the recovered signal in the n th iteration. If the error E is smaller than the threshold μ , the OMP iteration is finished, where μ is a small positive constant. Note that the smaller value of the threshold μ means that the smaller scattering coefficients will be recovered in the images. In this paper, the value of the threshold μ is chosen as 10^{-3} , which is small enough to extract the

domain scatterers reflectivity in the scene. Although simple and fast, OMP algorithm is empirically competitive in terms of approximation performance. It has been shown in [35] that the K -sparse signal \mathbf{x} can be exactly reconstructed by OMP with the measurements number $M \geq O(K \log(N/K))$ if the mutual coherence $\mu \leq 1/(2K - 1)$.

To recover a K -sparse M -elements signal with N -elements measurements, the computational complexity of the standard OMP strategies is about $O(KNM)$. In practice, the underlying 3-D scene usually consists of a huge number of cells, e.g., the number M will be one billion if the discrete 3-D scene size is $1000 \times 1000 \times 1000$. Moreover, the number of echo samples obtained by the 2-D antenna array is also very large, e.g., an 100×100 antenna array with 1000 sampling rate can produce ten million samples. In this case, the application of OMP algorithm for microwave 3-D imaging may suffer from very large computational complexity. In this paper, as seen from (8) in Section 2, we divide the underlying 3-D scene into a series of equality-range 2-D slices, and recover the reflection coefficients of these slices separately by OMP. If the 3-D scene is divided into P equality-range 2-D slices, the size, the measurements number and the sparsity of each slice will be only $1/P$ of the original 3-D scene. Then the computational complexity of the OMP can be reduced to $O(KNM/P^2)$, which is much smaller than $O(KNM)$. Therefore, the equality-range slice segmentation can significantly reduce the computation of the OMP recovery in microwave 3-D imaging.

3.3. The Performance Metrics

Since the true 3-D images of the underlying scenes are not available in our experiments, here we use two quality metrics, the target-to-background ratio (TBR) and the entropy of image (ENT) [36], to quantitatively evaluate the performance of the recovered images.

The TBR is defined as

$$\text{TBR} = 20 \log \left(\frac{N_{\mathbf{B}} \sum_{i \in \mathbf{T}} (|(\boldsymbol{\alpha})_i|)}{N_{\mathbf{A}} \sum_{j \in \mathbf{B}} (|(\boldsymbol{\alpha})_j|)} \right) \quad (16)$$

where \mathbf{T} denotes the target region and \mathbf{B} denotes the background region, $N_{\mathbf{A}}$ is the number of pixels in the target region, $N_{\mathbf{B}}$ is the number of pixels in the background region. A higher TBR value indicates that the target is easier to extract from its local background.

The ENT is a statistical measure that can be used to characterize the texture of the image, which is defined as

$$\text{ENT} = - \sum_{i=1}^G p(i) \log_2(p(i)) \quad (17)$$

where $p(i)$ denotes the gray level intensity histogram of the image, G is the number of levels in the histogram. A smaller ENT value means a sharper image.

4. EXPERIMENTAL RESULTS

In order to evaluate the performance of CS recovery in sparse array microwave 3-D imaging, some experiments for different types of targets were conducted by the developed microwave array 3-D imaging system. The system works on X-band with carrier frequency $f_c = 9.62$ GHz, signal bandwidth about $B = 120$ MHz and pulse repetition frequency $PRF = 20$ Hz. In these experiments, we employ the motion control module to synthesize three types of 2-D antenna arrays, and all the effective lengths of them are $1\text{ m} \times 1\text{ m}$. One is a dense 2-D array with its elements are obeyed by a periodic triangle distribution, as shown in Figure 2(a), it's activate elements number is 8000. The other two are sparse 2-D antenna arrays with their elements are followed by a random distribution, which are displayed in Figures 2(b) and (c), their activate elements numbers are 2000 and 500, respectively. Note that the sensor motion errors in these experiments have been effectively corrected by the phase gradient autofocus algorithm.

Figure 3 shows the mutual coherence of the measurement matrix for these 2-D antenna arrays via various intervals of the adjacent scene grids. These mutual coherences are similar to their system PSFs, the values will decrease if the interval of the adjacent scene grids increases. Obviously, a bigger scene grid means a lower value of mutual coherence, which can guarantee the performance of CS recovery

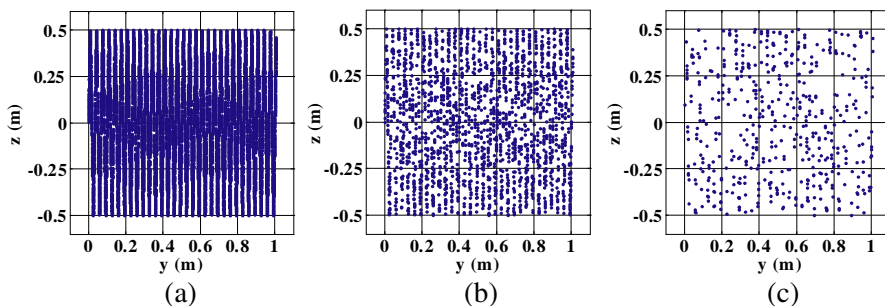


Figure 2. The three 2-D array used in the experiments. (a) The periodic triangle distribution dense array with 8000 elements. (b) The random distribution sparse array with 2000 elements. (c) The random distribution sparse array with 500 elements.

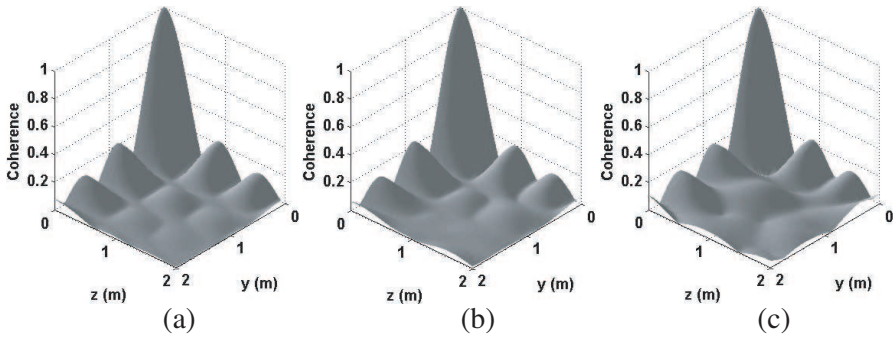


Figure 3. The mutual coherence of the measurement matrix via the space of the scene grid. (a) The periodic triangle distribution dense array with 8000 elements. (b) The random distribution sparse array with 2000 elements. (c) The random distribution sparse array with 500 elements.

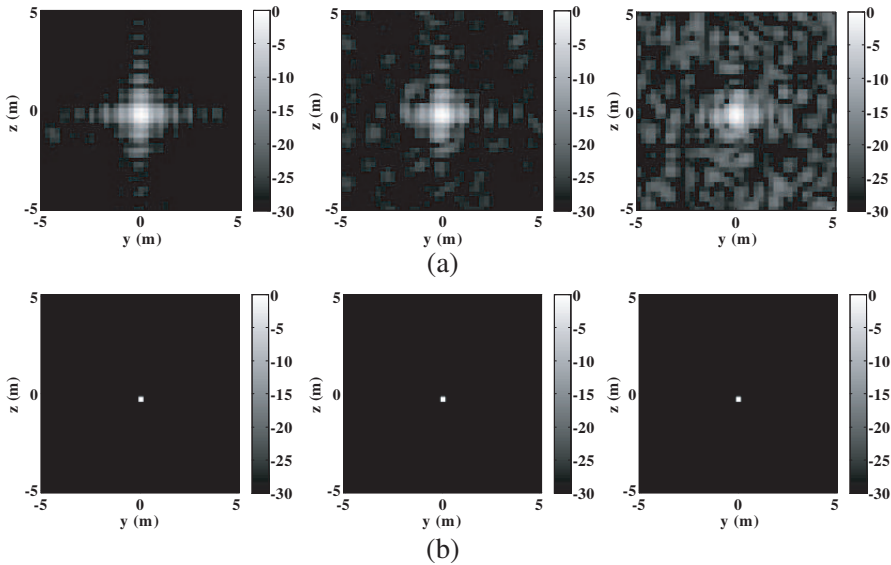


Figure 4. The reconstructed results of the single point target in the array plane. (a) The conventional BP algorithm. (b) The OMP algorithm. Left: the dense 2-D array with 8000 elements, middle: the sparse 2-D array with 2000 elements, right: sparse 2-D array with 500 elements.

with higher probability. But a large scene grid also can cause a low resolution. Hence, the space of scene cells should be properly selected based on these distributions of the mutual coherence and the image

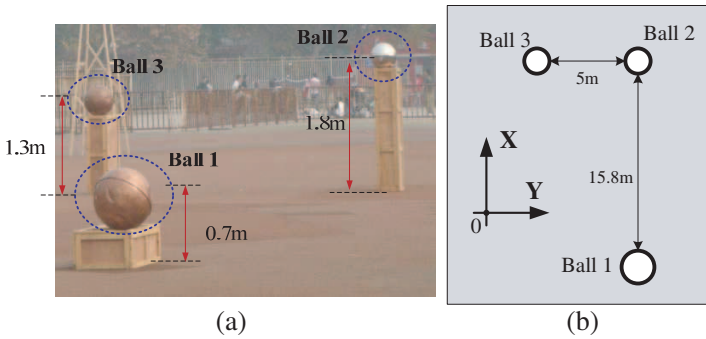


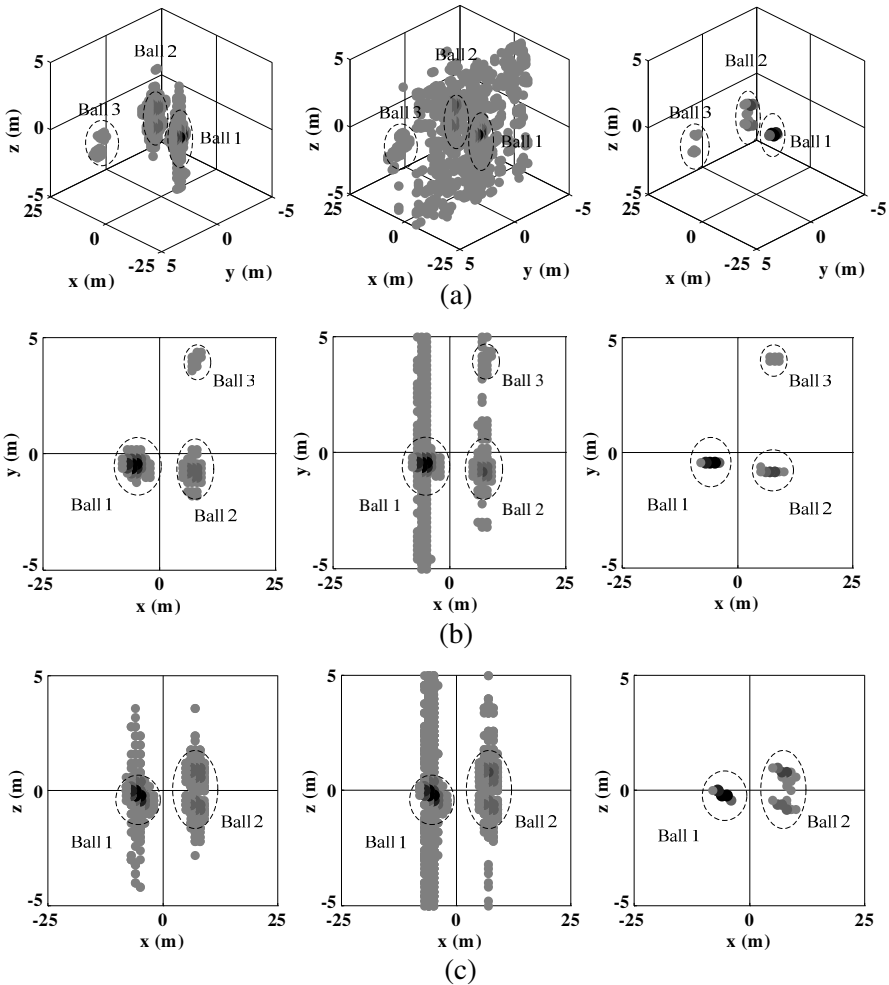
Figure 5. The three balls scene. (a) The photograph. (b) The geometrical model.

resolution. Commonly, to obtain a low mutual coherence and keep CS reconstruction successfully, the space of the adjacent scene cells should be larger than half of the nominal Rayleigh resolution (the 3 dB width of system's PSF), but smaller than the nominal Rayleigh resolution.

In the first experiment, the underlying scene consists of only one small copper ball. The distance from this ball to the antenna array platform is about 50 m, so the ball can be seen as an ideal single-point scatterer. The reconstructed images of this ball on the 2-D array plane by the conventional BP and the OMP algorithms, obtained from the above three different 2-D antenna arrays, are shown in Figures 4(a) and (b), respectively. The size of these images is 51×51 , and the interval of adjacent cells is 0.2m. From Figure 4, we can see that the conventional BP algorithm suffers from high side-lobes and low resolution, especially when the antenna array is very sparse with 500 elements, the ball is almost flooded in the sidelobes and very difficult to be distinguished. However, the OMP algorithm can reconstruct the single-point ball correctly, even if the array is extremely sparse with only 500 elements, its result still outperforms the conventional BP image obtained from the dense antenna array.

In the second experiment, the observed scene consists of three balls, one is copper and the other two are irons. The scene's photograph and the geometric model are displayed in Figures 5(a) and (b), respectively. The range from the ball 1 to the array antenna platform is approximate 25 m. The nominal Rayleigh resolution at this range is about $\rho_{xy} = \lambda R / (2L) \approx 0.39$ m. The ball 1 (the copper ball) is larger than the ball 2 and 3 (the irons ball), so the reflectivity of the ball 1 should be stronger than the other two balls in the recovered image. The 3-D scene space is divided into $51 \times 51 \times 41$ cells with 0.2m grid on the y - z plane and 1m grid x axis. The 3-D reconstructed

results of the BP and the OMP algorithms, obtained by the dense antenna array in Figure 2(a) and the sparse antenna array in Figure 2 (b), are demonstrated in Figure 6(a). The left and middle images are the BP results from the dense and the sparse arrays, and the right image is the OMP result from the sparse array. In these images, only the top 25 dB magnitude cells are displayed, and the darker color corresponds to the larger value. To observe clearly in each direction, the top view, the side view and the front view of these 3-D images are shown in Figures 6(b) to (d), respectively. Note that there are two dominate strong scatterers in the ball 2 and ball 3 positions due to the reflectivity of the wooden supports. As seen from Figure 6, the



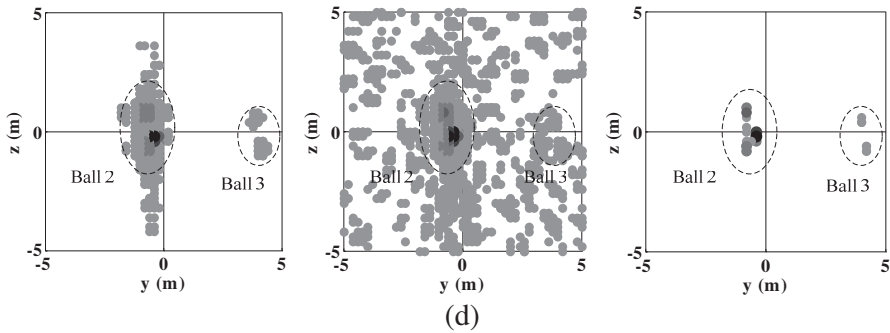


Figure 6. The reconstructed results of the three balls. (a) The 3-D images. (b) The top view images. (c) The side view images. (d) The front view images. Left: the BP results from the dense 2-D array with 8000 elements, middle: the BP results from the sparse 2-D array with 2000 elements, right: the OMP results from the sparse 2-D array with 2000 elements.

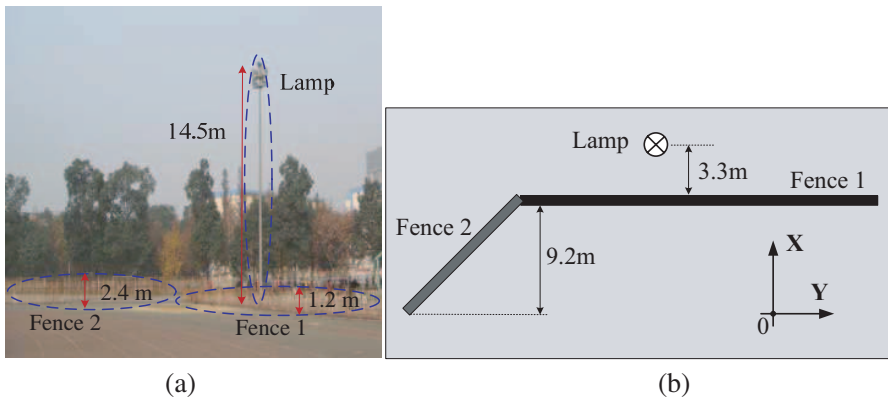


Figure 7. The lamp and fences scene. (a) The photograph. (b) The geometrical model.

conventional BP can distinguish the three balls when the 2-D antenna array is dense with 8000 elements. However, when the antenna array becomes a sparse array with only 2000 elements, the BP algorithm is difficult to extract the three balls in the recovered image due to the high side-lobes interference. In contrast to BP, the reconstructed images from the OMP algorithm can significantly suppress the high side-lobes and well capture the features of the three balls, e.g., their heights, locations and distances are similar to the actual measured values, which is useful for target detection and recognition. Further, it

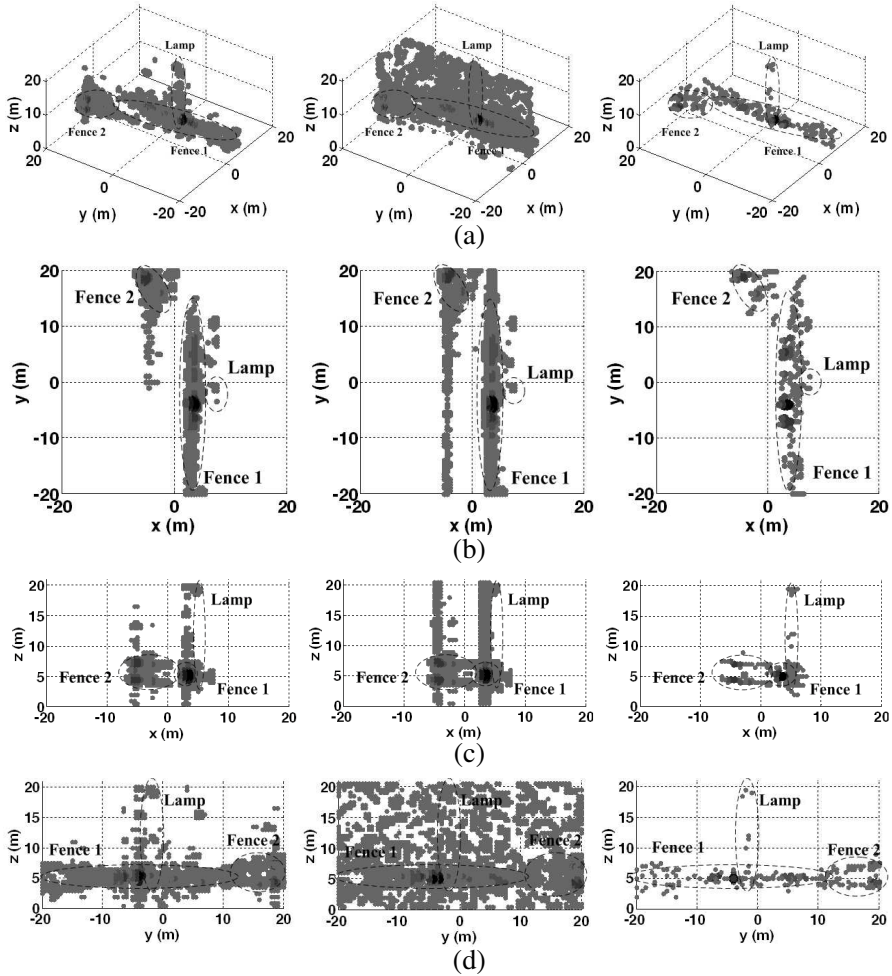


Figure 8. The reconstructed results of the lamp and fences scene. (a) The 3-D images. (b) The top view images. (c) The side view images. (d) The front view images. Left: the BP results from the dense 2-D array with 8000 elements, middle: the BP results from the sparse 2-D array with 2000 elements, right: the OMP results from the sparse 2-D array with 2000 elements.

can be obviously observed that the reflectivity of the ball 1 is stronger than the ball 2 and 3, which fits their physical truth.

In the third experiment, the underlying scene consists of a lamp and two metal fences, its photograph and geometric model are shown in Figures 7(a) and (b), respectively. These targets can be seen as

multiple-points scatterers. The distance between the lamp and the antenna array is about 107 m. The 2-D antenna array employed here is the same as that in the second experiment. Figure 8(a) shows the 3-D reconstructed images from the conventional BP and the OMP, respectively. The top 25 dB magnitude cells are displayed. The size of these 3-D images is $81 \times 41 \times 41$, and each grid is 0.5 m. The top view, the side view and the front view of these recovered 3-D images are shown in Figures 8(b) to (d), respectively. From Figure 8, we can clearly see that the proposed OMP algorithm provides a better reconstruction for the lamp and the fences compared to the conventional BP algorithm, especially in the case of the sparse 2-D antenna array with only 2000 elements. In addition, from the OMP images we can clearly distinguish the tops and bottoms of the lamp and the fence 2, and also easily obtain that the heights of the lamp is about 14.5 m and the height of the fence 2 is about 2.4 m, which are very close to their real heights. Hence, based on the observation that the observed targets usually exhibit spatial sparsity, the scatterer imaging can be converted into a sparse signal reconstruction problem. With this idea, microwave array system can provide a high-quality 3-D image of the underlying targets even if the 2-D antenna array is very sparse. These results may have a significant effect for many microwave imaging applications where the number of the antenna array elements is limited.

The quantitative evaluation of the above second and third experiments with TBR and ENT is given in Table 1. We find that the TBR decreases and the ENT increases for the BP results when the number of the antenna array elements decreases, but these metrics almost never change for the OMP results. Moreover, the OMP algorithm provides much higher TBR and lower ENT than the conventional BP algorithm, which means that the OMP improves the quality of reconstructed image and obtains a sharper image compared with the classical BP algorithm.

Table 1. Evaluation results of the experiments.

| Metrics | | The second experiment | | The third experiment | |
|---------|------------------|-----------------------|----------|----------------------|----------|
| | | BP (dB) | OMP (dB) | BP (dB) | OMP (dB) |
| TBR | The dense array | 43.92 | 81.33 | 37.25 | 69.98 |
| | The sparse array | 38.88 | 81.31 | 33.22 | 69.97 |
| ENT | The dense array | 2.063 | 0.012 | 2.907 | 0.043 |
| | The sparse array | 2.732 | 0.013 | 3.618 | 0.043 |

5. CONCLUSIONS

In this paper, we present a sparse array microwave 3-D imaging technique that employs a compressed sensing algorithm to reconstruct the 3-D image. Unlike the traditional system requires a dense 2-D array, we only randomly activate a small number of the elements to synthesize a sparse 2-D antenna array. By exploiting the typical sparsity in 3-D image, we pose the 3-D imaging as finding the sparse solutions to the under-determined linear equations constructed by the sparse array measurements. To avoid the large computation of the 3-D space recovery, we divide the scene into a series of equal-range 2-D slices. Finally, experimental results from an X-band microwave array imaging system are presented to validate the feasibility and the capability of the sparse array microwave 3-D imaging based on CS reconstruction. The results demonstrate that the presented CS algorithm can produce high-quality 3-D images with enhanced resolution and suppressed sidelobes, and also can maintain the targets' features well compared with the conventional methods. Our results make the sparse array possible to be applied in high-quality and low-cost microwave imaging system. It also can be an example for many other similar imaging systems, such as sonar and acoustic imaging, etc..

ACKNOWLEDGMENT

This work was supported by the Fundamental Research Funds for the Central Universities (No. E022050205) and the Doctoral Fund of Ministry of Education of China (No. 20110185110001). The authors thank the anonymous reviewers for their valuable comments to improve the paper quality.

REFERENCES

1. Peng, X., W. Tan, Y. Wang, W. Hong, and Y. Wu, "Convolution back-projection imaging algorithm for downward-looking sparse linear array three dimensional synthetic aperture radar," *Progress In Electromagnetics Research*, Vol. 129, 287–313, 2012.
2. Mohammadpoor, M., R. S. A. Raja Abdullah, A. Ismail, and A. F. Abas, "A circular synthetic aperture radar for on-the-ground object detection," *Progress In Electromagnetics Research*, Vol. 122, 269–292, 2012.
3. Tan, W., W. Hong, Y. Wang, and Y. Wu, "A novel spherical-wave three-dimensional imaging algorithm for microwave cylindrical

- scanning geometries,” *Progress In Electromagnetics Research*, Vol. 111, 43–70, 2011.
4. Huang, Y., Y. Liu, Q. H. Liu, and J. Zhang, “Improved 3-d GPR detection by NUFFT combined with MPD method,” *Progress In Electromagnetics Research*, Vol. 103, 185–199, 2010.
 5. Deng, M. Y. and X. Liu, “Electromagnetic imaging methods for nondestructive evaluation applications,” *Sensors*, Vol. 11, No. 12, 11774–11808, 2011.
 6. Zhou, H., T. Takenaka, J. Johnson, and T. Tanaka, “A breast imaging model using microwaves and a time domain three dimensional reconstruction method,” *Progress In Electromagnetics Research*, Vol. 93, 57–70, 2009.
 7. Wei, H.-Y. and M. Soleimani, “Three dimensional magnetic induction tomography imaging using a matrix free Krylov subspace inversion algorithm,” *Progress In Electromagnetics Research*, Vol. 122, 2945, 2012.
 8. Soleimani, M., C. N. Mitchell, R. Banasiak, R. Wajman, and A. Adler, “Four-dimensional electrical capacitance tomography imaging using experimental data,” *Progress In Electromagnetics Research*, Vol. 90, 171–186, 2009.
 9. Ren, X. Z., L. H. Qiao, and Y. Qin, “A three-dimensional imaging algorithm for tomography SAR based on improved interpolated array transform1,” *Progress In Electromagnetics Research*, Vol. 120, 181–193, 2011.
 10. Liao, K. F., X.-L. Zhang, and J. Shi, “Fast 3-d microwave imaging method based on subaperture approximation,” *Progress In Electromagnetics Research*, Vol. 126, 333–353, 2012.
 11. Yu, L. and Y. Zhang, “A 3D target imaging algorithm based on two-pass circular SAR observations,” *Progress In Electromagnetics Research*, Vol. 122, 341–360, 2012.
 12. Shi, J., X.-L. Zhang, J.-Y. Yang, et al., “APC trajectory design for ‘One-Active’ linear-array three-dimensional imaging SAR,” *IEEE Transactions on Geoscience and Remote Sensing*, Vol. 48, No.3, 1470–1486, 2010.
 13. Shi, J., X. L. Zhang, J. Yang, and K. Liao, “Experiment results on one-active LASAR,” *IEEE Radar Conference*, 1–4, 2009.
 14. Juan, L. S. and F. G. Joaquim, “3-D radar imaging using range migration techniques,” *IEEE Transactions on Antennas and Propagation*, Vol. 48, No. 5, 2000.
 15. Zhang, D. H. and X. L. Zhang, “Downward-looking 3-D linear array SAR imaging based on chirp scaling algorithm,” *Asian-*

- Pacific Conference on SAR*, 1043–1046, 2009.
16. Qi, Y., W. Tan, Y. Wang, W. Hong, and Y. Wu, “3D bistatic omega-k imaging algorithm for near range microwave imaging systems with bistatic planar scanning geometry,” *Progress In Electromagnetics Research*, Vol. 121, 409–431, 2011.
 17. Li, S., B. Ren, H.-J. Sun, W. Hu, and X. Lv, “Modified wavenumber domain algorithm for three-dimensional millimeter-wave imaging,” *Progress In Electromagnetics Research*, Vol. 124, 35–53, 2012.
 18. Montefusco, L. B., D. Lazzaro, S. Papi, and C. Guerrini, “A fast compressed sensing approach to 3D MR image reconstruction,” *IEEE Transactions on Medical Imaging*, Vol. 30, No. 5, 2011.
 19. Berger, C. R., S. L. Zhou, J. C. Preisig, and P. Willett, “Sparse channel estimation for multicarrier underwater acoustic communication: From subspace methods to compressed sensing” *IEEE Transactions on Signal Processing*, Vol. 58, No. 3, 2010.
 20. Mahalanobis, A. and R. Muise, “Object specific image reconstruction using a compressive sensing architecture for application in surveillance systems,” *IEEE Transactions on Aerospace and Electronic System*, Vol. 45, No. 3, 2009.
 21. Wei, S.-J., X.-L. Zhang, J. Shi, and G. Xiang, “Sparse reconstruction for SAR imaging based on compressed sensing,” *Progress In Electromagnetics Research*, Vol. 109, 63–81, 2010.
 22. Patel, V. M., G. R. Easley, and D. M. Healy, “Compressed synthetic aperture radar,” *IEEE Journal of Selected Topics in Signal Processing*, Vol. 4, No. 2, 244–254, 2010.
 23. Zhu, X.-X. and R. Bamler, “Tomographic SAR inversion by L_1 -norm regularization the compressive sensing approach,” *IEEE Transactions on Geoscience and Remote Sensing*, Vol. 48, No. 10, 3839–3846, 2010.
 24. Budillon, A., A. Evangelista, and G. Schirinzi, “Three-dimensional SAR focussing from multipass signals using compressive sampling,” *IEEE Transactions on Geoscience and Remote Sensing*, Vol. 49, No. 1, 488–499, 2010.
 25. Chen, J., J. Gao, Y. Zhu, W. Yang, and P. Wang, “A novel image formation algorithm for high-resolution wide-swath spaceborne SAR using compressed sensing on azimuth displacement phase center antenna,” *Progress In Electromagnetics Research*, Vol. 125, 527–543, 2012.
 26. Li, J., S. Zhang, and J. Chang, “Applications of compressed

- sensing for multiple transmitters multiple azimuth beams SAR imaging,” *Progress In Electromagnetics Research*, Vol. 127, 259–275, 2012.
27. Oliveri, G., P. Rocca, and A. Massa, “A Bayesian-compressive-sampling-based inversion for imaging sparse scatterers,” *IEEE Transactions on Geoscience and Remote Sensing*, Vol. 49, No. 10, 3993–4006, 2011.
 28. Poli, L., G. Oliveri, and A. Massa, “Microwave imaging within the first-order born approximation by means of the contrast-field Bayesian compressive sensing,” *IEEE Transactions on Antennas and Propagation*, Vol. 60, No. 6, 2865–2879, 2012.
 29. Wei, S.-J., X.-L. Zhang, and J. Shi, “Linear array SAR imaging via compressed sensing,” *Progress In Electromagnetics Research*, Vol. 117, 299–319, 2011.
 30. Donoho, D., “Compressed sensing,” *IEEE Trans. Inf. Theory*, Vol. 52, No. 4, 1289–1306, 2006.
 31. Candes, E. J. and M. Wakin, “An introduction to compressive sampling,” *IEEE Signal Processing Magazine*, 21–30 2008.
 32. Candes, E. J., J. K. Romberg, and T. Tao, “Robust uncertainty principles: Exact signal reconstruction from highly incomplete frequency information,” *IEEE Trans. Inf. Theory*, Vol. 52, No. 2, 489–509, 2006.
 33. Tropp, J. A., “Greed is good: Algorithm results for sparse approximation,” *IEEE Trans. Inf. Theory*, Vol. 50, No. 10, 2231–2242, 2004.
 34. Needell, D. and R. Vershynin, “Uniform uncertainty principle and signal recovery via regularized orthogonal matching pursuit,” *Found. Comput. Math.*, Vol. 9, No. 3, 317–334, 2009.
 35. Fornasier, M. and H. Rauhut, “Compressive sensing,” *Handbook of Mathematical Methods in Imaging*, Vol. 1, 187–229, Springer, 2010.
 36. Samadi, S., M. Çetin, and M. A. Masnadi-Shirazi, “Sparse representation-based synthetic aperture radar imaging,” *IET Radar, Sonar and Navigation*, Vol. 5, No. 2, 182–193, 2011.